

Image charges in spherical geometry: Application to colloidal systems

René Messina*

Max-Planck-Institut für Polymerforschung, Ackermannweg 10, 55128 Mainz, Germany

(Dated: October 29, 2018)

The effects of image charges (i.e., induced surface charges of polarization) in spherical geometry and their implication for charged colloidal systems are investigated. We study analytically and exactly a single microion interacting with a dielectric sphere and discuss the similarities and discrepancies with the case of a planar interface. By means of extensive Monte Carlo (MC) simulations, we study within the framework of the primitive model the effects of image charges on the structure of the electrical double layer. Salt-free environment as well as salty solutions are considered. A remarkable finding of this study is that the position of the maximum in the counterion density (appearing at moderately surface charge density) remains quasi-identical, regardless of the counterion valence and the salt content, to that obtained within the *single*-counterion system.

PACS numbers: 61.20.Qg, 82.70.Dd, 41.20.Cv

I. INTRODUCTION

In charged colloidal systems electrostatic effects, and especially the structure of the electrical double layer, often play a crucial role in determining their physico-chemical properties. It is well known that charged colloids (i.e., macroions) have typically a low dielectric constant ($\varepsilon_r \approx 2 - 5$) which is much smaller than that of the surrounding solvent (e.g., for water $\varepsilon_r \approx 80$). In most of the theoretical works, this dielectric discontinuity is ignored.

Nevertheless, a few studies have addressed the effects of image charges (i.e., image forces stemming from the dielectric discontinuity) on the counterion distribution for planar geometry which is closely related to our problem. An electrolyte close to a charged wall^{1,2} or confined between two charged plates³ had been the subject of MC simulations. Similar systems have also been investigated by integral-equation^{4,5,6} and mean field theories.^{7,8,9}

As far as the spherical geometry is concerned, much less literature is available. Counterion distributions with image forces in salt-free environment had been investigated by MC simulations.¹⁰ There an oversimplified approximation for the treatment of the image forces was used. The main conclusions however remain correct on a very qualitative level of description.

The aim of this paper is to provide a detailed analysis of the image forces in spherical geometry and their effects on the structure of the electrical double layer. The remainder of this article is set out as follows. Section II corresponds to the analytical part of the paper. We first briefly present the general theoretical background of the concept of image charges in spherical geometry. Then we apply it to colloidal systems to compute (exactly) some relevant observables and discuss our results. Section III is devoted to the computational details of our MC simulations. In Sec. IV we present our simulation results for salt-free environment as well as salty solutions where image forces are explicitly taken into account with no approximation. Finally, Sec. V contains brief concluding remarks.

II. THEORY

In this part we mainly study the interaction of a *single excess* charge with a dielectric sphere. We briefly present the formalism of the dielectric model for spherical interfaces and discuss some important electrostatic properties. Such a system captures the underlying physics of image forces in spherical geometry. Moreover, a systematic quantitative comparison with the planar geometry is undertaken.

A. Poisson equation with azimuthal symmetry

The model system is sketched in Fig. 1. Consider an *uncharged* dielectric sphere of radius a and dielectric constant (relative permittivity) ε_2 embedded in an infinite dielectric medium (region 1) characterized by ε_1 . A single excess charge of magnitude q is located outside the dielectric sphere at a distance $b = |\mathbf{b}|$ from its center.

The central problem is to determine the electrostatic potential $\Phi(\mathbf{r})$ at any point in the space. This is achieved by solving the Poisson equation which reads

$$\Delta\Phi(\mathbf{r}) = -\frac{\rho(\mathbf{r})}{\varepsilon}, \quad (1)$$

where $\rho(\mathbf{r})$ is the volume charge density and $\varepsilon = \varepsilon_0\varepsilon_i$ with ε_0 being the vacuum permittivity and $i = 1, 2$. Since here $\rho(\mathbf{r}) = q\delta(\mathbf{r} - \mathbf{b})$ and taking into account the azimuthal symmetry, Eq. (1) reduces (for $\mathbf{r} \neq \mathbf{b}$) to the Laplace equation

$$\Delta\Phi(r, \theta) = \frac{1}{r^2} \frac{\partial}{\partial r} \left(r^2 \frac{\partial\Phi}{\partial r} \right) + \frac{1}{r^2 \sin\theta} \frac{\partial}{\partial\theta} \left(\sin\theta \frac{\partial\Phi}{\partial\theta} \right) = 0, \quad (2)$$

where θ is the angle between \mathbf{r} and \mathbf{b} (see Fig. 1) and $r = |\mathbf{r}|$. The general solution of the Laplace equation with azimuthal symmetry is given by^{12,13,14}

REGION 1

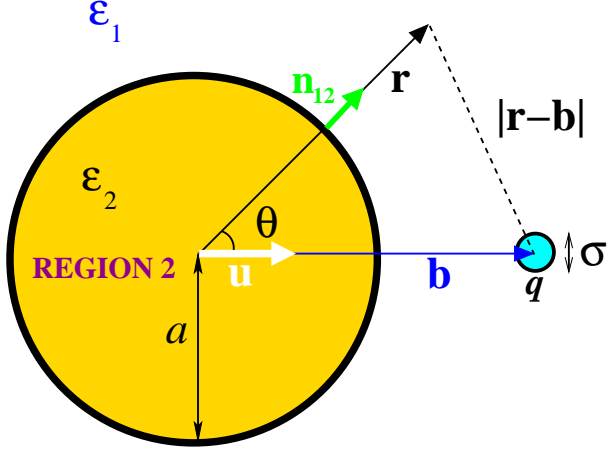


FIG. 1: Model for a dielectric sphere (colloid) of dielectric constant ϵ_2 embedded in an infinite medium characterized by a different dielectric constant ϵ_1 . An excess charge (q) is located near the boundary outside the spherical particle. This is a two-dimensional representation of the three-dimensional system.

$$\Phi(r, \theta) = \sum_{l=0}^{\infty} \left[M_l r^l + N_l \frac{1}{r^{l+1}} \right] P_l(\cos \theta), \quad (3)$$

where $P_l(\cos \theta)$ is the associated Legendre polynomial of order l .

Inside the dielectric sphere (region 2) the electrostatic potential $\Phi_2(\mathbf{r})$ must be finite at $r = 0$ so that $N_l = 0$ in Eq. (3), and hence

$$\Phi_2(r, \theta) = \sum_{l=0}^{\infty} A_l r^l P_l(\cos \theta). \quad (4)$$

Concerning the electrostatic potential outside the dielectric sphere (region 1) we know that without dielectric discontinuity (at $r = a$) the potential would simply be given by $\frac{q}{4\pi\epsilon_0\epsilon_1|\mathbf{r}-\mathbf{b}|}$. Making use of the following identity

$$\frac{1}{|\mathbf{r} - \mathbf{b}|} = \sum_{l=0}^{\infty} \frac{r_{<}^l}{r_{>}^{l+1}} P_l(\cos \theta), \quad (5)$$

where $r_{<} (r_{>})$ is the smaller (larger) of r and b , the electrostatic potential $\Phi_1(\mathbf{r})$ in region 1 reads¹¹

$$\Phi_1(r, \theta) = \sum_{l=0}^{\infty} \left[C_l \frac{1}{r^{l+1}} + \frac{q}{4\pi\epsilon_0\epsilon_1} \frac{r_{<}^l}{r_{>}^{l+1}} \right] P_l(\cos \theta), \quad (6)$$

recalling that $\Phi_1(\mathbf{r})$ must be finite at $r \rightarrow \infty$ so that $M_l = 0$ in Eq. (3).

B. Boundary conditions

The electrostatic potentials given by Eqs. (4) and (6) will be univocally determined by applying the proper boundary conditions that will fix A_l and C_l . The boundary conditions are derived from the full set of Maxwell equations. The results are that the normal components of the displacement \mathbf{D} and the tangential components of \mathbf{E} on either side of the spherical interface at $r = a$ satisfy

$$\begin{cases} (\mathbf{D}_1 - \mathbf{D}_2) \cdot \mathbf{n}_{12} = 0 \\ (\mathbf{E}_1 - \mathbf{E}_2) \times \mathbf{n}_{12} = 0 \end{cases} \quad (7)$$

where $\mathbf{n}_{12} = \mathbf{r}/r$ is a unit normal vector to the surface directed from region 2 to region 1 (see Fig. 1). Within the framework of the linear response theory we have $\mathbf{D} = \epsilon \mathbf{E}$. Combining Eqs. (4) and (6) with Eq. (7) and noting that $\mathbf{E} = -\nabla\Phi$, it follows that

$$\begin{cases} \epsilon_2 A_l l a^{l-1} = \epsilon_1 \left[-C_l \frac{l+1}{a^{l+2}} + \frac{q}{4\pi\epsilon_0\epsilon_1} \frac{l a^{l-1}}{b^{l+1}} \right] \\ A_l a^l = C_l \frac{1}{a^{l+1}} + \frac{q}{4\pi\epsilon_0\epsilon_1} \frac{a^l}{b^{l+1}} \end{cases} \quad (8)$$

This set of two equations [Eq. (8)] can be readily solved to yield the Legendre coefficients A_l and C_l :

$$\begin{cases} A_l = \frac{q}{4\pi\epsilon_0\epsilon_1} \frac{1}{b^{l+1}} \frac{\epsilon_1(2l+1)}{\epsilon_1(l+1) + \epsilon_2 l} \\ C_l = \frac{q}{4\pi\epsilon_0\epsilon_1} \frac{a^{2l+1}}{b^{l+1}} \frac{(\epsilon_1 - \epsilon_2)l}{\epsilon_1(l+1) + \epsilon_2 l} \end{cases} \quad (9)$$

and hence

$$\Phi_1(r, \theta) = \frac{q}{4\pi\epsilon_0\epsilon_1} \times \left[\frac{1}{|\mathbf{r} - \mathbf{b}|} + \sum_{l=1}^{\infty} \frac{a^{2l+1}}{b^{l+1}} \frac{(\epsilon_1 - \epsilon_2)l}{\epsilon_1(l+1) + \epsilon_2 l} \frac{1}{r^{l+1}} P_l(\cos \theta) \right]. \quad (10)$$

The physical interpretation of Eq. (10) is straightforward. The first term represents the usual electrostatic potential (without image forces) generated by q and the second term can be referred to as the electrostatic potential due to “image charges” stemming from the dielectric discontinuity. As expected, the strength of the image force is strongly governed by the jump $\Delta\epsilon$ in the dielectric constant defined as

$$\Delta\epsilon = \epsilon_1 - \epsilon_2. \quad (11)$$

In particular, one can anticipate and state that the interaction between the microion q and the dielectric particle

(i.e., the *self-image interaction*) is *repulsive* for $\Delta\varepsilon > 0$ (i.e., $\varepsilon_1 > \varepsilon_2$) and *attractive* for $\Delta\varepsilon < 0$ (i.e., $\varepsilon_1 < \varepsilon_2$) as it is also the case in planar geometry.

One can show that Eq. (10) can also be written as follows (see e.g., Ref.¹⁵ and references therein)

$$\Phi_1(r, \theta) = \frac{q}{4\pi\varepsilon_0\varepsilon_1} \left\{ \frac{1}{|\mathbf{r} - \mathbf{b}|} + \frac{\varepsilon_1 - \varepsilon_2}{\varepsilon_1 + \varepsilon_2} \frac{1}{a} \right. \\ \times \left[\frac{u}{|\mathbf{r} - \mathbf{u}|} - \frac{\varepsilon_1}{\varepsilon_1 + \varepsilon_2} \int_0^u \frac{(u/x)^{\varepsilon_2/(\varepsilon_1+\varepsilon_2)}}{|\mathbf{r} - \mathbf{x}|} dx \right] \left. \right\}, \quad (12)$$

where $\mathbf{u} = \mathbf{b}a^2/b^2$ (see Fig. 1).¹⁶ In this formalism the geometrical structure of the image charges is transparent and it is specified by the second main term (between brackets) of Eq. (12). More precisely, one has to deal with an *infinite manifold* of image charges distributed along the oriented segment \mathbf{u} that electrically compensates the image point-charge q_{im} located at \mathbf{u} and whose magnitude is given by

$$q_{im} = q \frac{\varepsilon_1 - \varepsilon_2}{\varepsilon_1 + \varepsilon_2} \frac{a}{b}. \quad (13)$$

C. Polarization charge

It is important to know the surface distribution of the induced charge on the spherical interface. In the bulk (i. e., in region 1 or 2) we have a zero volume density of polarization charge (ρ_{pol}) since $\rho_{pol} = \varepsilon_0 \nabla \cdot \mathbf{E} = -\nabla \cdot \mathbf{P} = 0$ (except at $\mathbf{r} = \mathbf{b}$). At the interface ($r = a$) the surface density of polarization charge $\sigma_{pol}^{(sph)}$ is given by

$$\sigma_{pol}^{(sph)} = -(\mathbf{P}_1 - \mathbf{P}_2) \cdot \mathbf{n}_{12}, \quad (14)$$

where

$$\begin{cases} \mathbf{P}_1 = \varepsilon_0(\varepsilon_1 - 1)\mathbf{E}_1 = -\varepsilon_0(\varepsilon_1 - 1)\nabla\Phi_1 \\ \mathbf{P}_2 = \varepsilon_0(\varepsilon_2 - 1)\mathbf{E}_2 = -\varepsilon_0(\varepsilon_2 - 1)\nabla\Phi_2 \end{cases} \quad (15)$$

are the polarizations in region 1 and 2, respectively. Using Eqs. (4), (6), (9), (14) and (15), the final expression of $\sigma_{pol}^{(sph)}$ reads

$$\sigma_{pol}^{(sph)}(\cos\theta) = \frac{q}{4\pi\varepsilon_1 b^2} \sum_{l=1}^{\infty} \left(\frac{a}{b} \right)^{l-1} (2l+1)l \\ \times \frac{\varepsilon_1 - \varepsilon_2}{\varepsilon_1(l+1) + \varepsilon_2 l} P_l(\cos\theta). \quad (16)$$

The net charge of polarization $Q_{pol}^{(sph)} = \int_{-1}^1 2\pi a^2 \sigma_{pol}^{(sph)}(\cos\theta) d(\cos\theta)$ is zero,¹⁷ meaning that there is *no monopole* contribution as it should be.

The critical angle θ^* where $\sigma_{pol}^{(sph)}$ changes sign is given by the geometrical condition

$$\begin{cases} \mathbf{E}_1(r = a, \theta^*) \perp \mathbf{n}_{12} \\ \mathbf{E}_2(r = a, \theta^*) \perp \mathbf{n}_{12} \end{cases} \quad (17)$$

which is the orthogonality condition at the interface between the (inner and outer) electric field and \mathbf{n}_{12} . In terms of Legendre polynomials, Eq. (17) can be equivalently written as

$$\sum_{l=1}^{\infty} \left(\frac{a}{b} \right)^{l-1} (2l+1)l \frac{\varepsilon_1 - \varepsilon_2}{\varepsilon_1(l+1) + \varepsilon_2 l} P_l(\cos\theta^*) = 0, \quad (18)$$

where Eq. (16) was used. Two limiting cases can be easily described: (i) for $b/a \gg 1$ we have $\theta^* \rightarrow \pi/2$ [recalling that $P_1(\cos\theta) = \cos\theta$] and (ii) for $b/a \rightarrow 1$ we have $\theta^* \rightarrow 0$. In general, θ^* increases with b and it is a complicated function of b/a , ε_1 and ε_2 .

For a *planar* interface, the surface density of polarization charge $\sigma_{pol}^{(plan)}(d)$ is given by¹⁴

$$\sigma_{pol}^{(plan)}(d) = \frac{q}{2\pi\varepsilon_1\varepsilon_1 + \varepsilon_2} \frac{\varepsilon_1 - \varepsilon_2}{[(b-a)^2 + d^2]^{3/2}}, \quad (19)$$

where $d = \sqrt{x^2 + y^2}$ is the radial distance (in cylindrical coordinates system) belonging to the planar interface (see Fig. 2). Equation (19) demonstrates that $\sigma_{pol}^{(plan)}(d)$ *never* changes sign [as can also be deduced from simple geometrical considerations - Eq. (17)] in contrast with the spherical interface. The total charge of polarization $Q_{pol}^{(plan)}$ is obtained by direct integration of $\sigma_{pol}^{(plan)}(d)$ and its expression is given by

$$Q_{pol}^{(plan)} = \frac{q'}{\varepsilon_1}, \quad (20)$$

where

$$q' = q \frac{\varepsilon_1 - \varepsilon_2}{\varepsilon_1 + \varepsilon_2} \quad (21)$$

is the *unique* image charge located at the mirror position of q (see Fig. 2). This *non-zero* monopolar contribution for the planar interface involves a *stronger* and *longer ranged* self-image interaction.

D. Application to colloidal systems

So far we treat in a rather general manner the physics of a point charge near a spherical dielectric interface. We now would like to apply the above theory to colloidal systems. In the remaining of this paper we suppose that

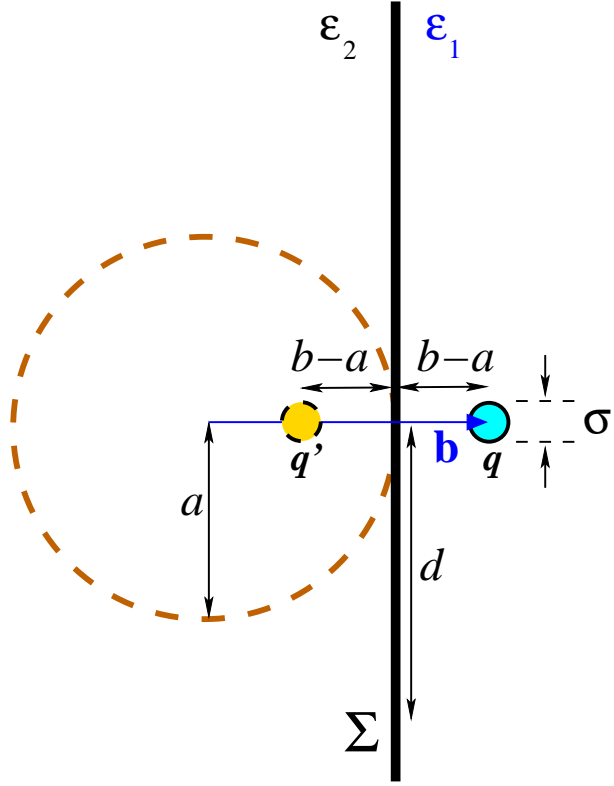


FIG. 2: Model for a microion (q) near a planar interface (Σ) separating the two infinite media characterized by ϵ_1 and ϵ_2 . The imaginary spherical dielectric of radius a is shown for geometrical comparison with the setup of Fig. 1. This is a two-dimensional representation of the three-dimensional system.

region 1 corresponds to water, so that we take $\epsilon_1 = 80$ corresponding to the water dielectric constant at room temperature. To characterize the low permittivity of the colloid we consider here $\epsilon_2 = 2$ so that $\Delta\epsilon = 78$. The little ion carries a charge $q = Ze$ where e stands for the elementary charge and Z for its valence, and has a diameter σ . An important quantity is

$$r_0 = a + \frac{\sigma}{2} \quad (22)$$

being the center-center distance of closest approach between the colloid and the microion q .

1. Induced surface charge

It is helpful to have a precise representation of the polar profile of $\sigma_{pol}^{(sph)}(\theta)$ in order to get a clear understanding of the source of the image forces. Although at first glance such a study should belong to standard electrostatics we are not aware of any data in the literature that treats this crucial aspect.

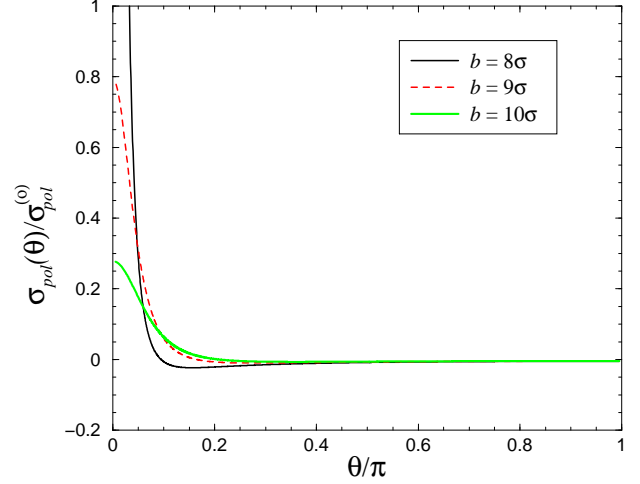


FIG. 3: Polar profile of the surface density of polarization charge $\sigma_{pol}^{(sph)}(\theta)$ in units of $\sigma_{pol}^{(0)} = \frac{q}{4\pi\epsilon_1\sigma^2}$ for different radial distances b of the excess charge q with $\epsilon_1 = 80$, $\epsilon_2 = 2$ and $a = 7.5\sigma$.

The numerical computation of Eq. (16) was performed using a cutoff $l_{max} = 300$ in the Legendre space leading to high accuracy.¹⁸ The plot of $\sigma_{pol}^{(sph)}(\theta)$ for $a = 7.5\sigma$ and $b/\sigma = 8, 9$ and 10 can be found in Fig. 3. One can clearly observe that $\sigma_{pol}^{(sph)}(\theta)$ is strongly *inhomogeneous*. For small θ , $\sigma_{pol}^{(sph)}(\theta)$ is highly positive (i.e., it carries the same charge sign as q) and decreases abruptly. The angle θ^* [given by Eq. (18)] where $\sigma_{pol}^{(sph)}(\theta)$ changes sign is 16.9° , 29.5° and 37.4° for $b/\sigma = 8, 9$ and 10 , respectively. In parallel, by increasing b one drastically decreases the magnitude as well as the inhomogeneity of $\sigma_{pol}^{(sph)}(\theta)$. Recall that for $b/a \gg 1$ we have $\sigma_{pol}^{(sph)}(\theta) \sim \cos\theta$.

It is insightful to compare $\sigma_{pol}^{(sph)}(\theta = 0)$ with $\sigma_{pol}^{(plan)}(d = 0)$ [computed from Eq. (19)] since both quantities give the maximum of $\sigma_{pol}^{(sph)}(\theta)$ and $\sigma_{pol}^{(plan)}(d)$, respectively. The corresponding numerical values are gathered in Table I. The values found at finite curvature are very similar to those of zero one. The fact that $\sigma_{pol}^{(sph)}(\theta = 0)$ is systematically smaller than $\sigma_{pol}^{(plan)}(d = 0)$ is consistent with the idea that in spherical geometry we have

TABLE I: Numerical values of $\sigma_{pol}^{(sph)}(\theta = 0)$ and $\sigma_{pol}^{(plan)}(d = 0)$ in units of $\frac{q}{4\pi\epsilon_1\sigma^2}$ as a function of b . The corresponding profiles of $\sigma_{pol}^{(sph)}(\theta)$ can be found in Fig. 3.

b/σ	$\sigma_{pol}^{(sph)}(\theta = 0)$	$\sigma_{pol}^{(plan)}(d = 0)$
8	7.41	7.61
9	0.794	0.846
10	0.278	0.304

the presence of opposite image charges. Nevertheless, for sufficiently large a one should recover the planar case.

2. Self-image interaction

We now compute the potential of interaction between the microion q and the dielectric particle or, in terms of image forces, the potential of self-image interaction. This is the work done in bringing the microion from infinity to its position \mathbf{b} , and it is equal to the *half*-product of q and the second term of $\Phi_1(r = b)$ given by Eq. (10). In that case we have $\mathbf{r} = \mathbf{b}$ (see Fig. 1), so that $\theta = 0$ and therefore $P_l[\cos(\theta = 0)] = 1$. In order to normalize the energy with $k_B T$ we introduce the Bjerrum length $l_B = e^2/(4\pi\epsilon_0\epsilon_1 k_B T)$ which is 7.14 Å for water at $T = 298$ K. By choosing $\sigma = 3.57$ Å we have $l_B = 2\sigma$. The potential of self-image interaction $V_{self}^{(sph)}(b)$ is then given by

$$V_{self}^{(sph)}(b) = \frac{1}{2}k_B T l_B \frac{Z^2}{b} \sum_{l=1}^{\infty} \left(\frac{a}{b}\right)^{2l+1} \frac{(\epsilon_1 - \epsilon_2)l}{\epsilon_1(l+1) + \epsilon_2 l}. \quad (23)$$

Equation (23) shows that the typical interaction range scales like $1/b^4$ and therefore it is *short-ranged*.¹⁹ Note that it is fully equivalent to compute $V_{self}^{(sph)}(b)$ from the surface polarization charges as follows

$$V_{self}^{(sph)}(b) = \frac{1}{2} \frac{1}{4\pi\epsilon_0} \int_{-1}^1 2\pi a^2 q \frac{\sigma_{pol}^{(sph)}(\cos\theta)}{|\mathbf{r}_a - \mathbf{b}|} d(\cos\theta), \quad (24)$$

where \mathbf{r}_a is the radial vector of magnitude $|\mathbf{r}_a| = a$ and $\sigma_{pol}^{(sph)}(\cos\theta)$ is given by Eq. (16).

It is insightful to compare the potential of self-image interaction obtained in spherical geometry with that, $V_{self}^{(plan)}(b - a)$, obtained in planar geometry. The setup for a planar interface is sketched in Fig. 2. In this situation the analytical expression of $V_{self}^{(plan)}(b - a)$ is simply given by

$$V_{self}^{(plan)}(b - a) = \frac{1}{2}k_B T l_B Z^2 \frac{\epsilon_1 - \epsilon_2}{\epsilon_1 + \epsilon_2} \frac{1}{2(b - a)}. \quad (25)$$

Profiles of $V_{self}^{(sph)}(b)$ (for two colloidal radii) and $V_{self}^{(plan)}(r)$ are reported in Fig. 4. Since in both (planar and spherical) cases the potential of interaction diverges at the interface, we only show results from $r > r_0$ as it is the case in experimental systems. The numerical computation of Eq. (23) was performed using the formalism of Eq. (12) allowing an arbitrary precision.²⁰

Figure 4 clearly shows that the self-image interaction is weaker (the higher the curvature) with a spherical interface than with a planar one. In particular, at

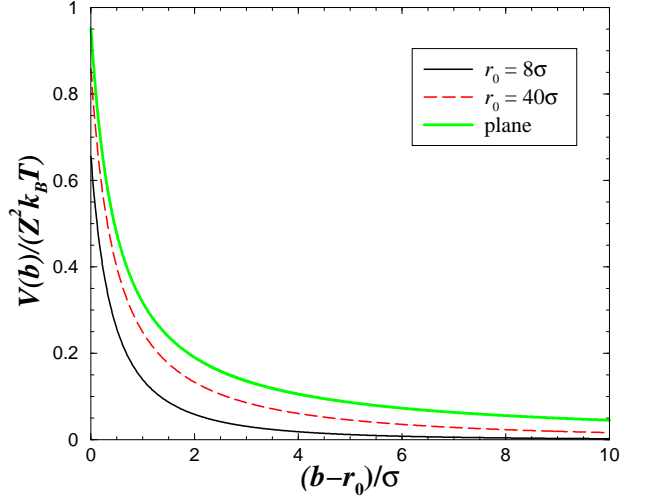


FIG. 4: Potential of self-image interaction for a microion ($q = Ze$) in spherical and planar geometries with $\epsilon_1 = 80$ and $\epsilon_2 = 2$.

contact we have $V_{self}^{(sph)}(r_0 = 8\sigma) = 0.66Z^2 k_B T$ and $V_{self}^{(sph)}(r_0 = 40\sigma) = 0.86Z^2 k_B T$ for the spherical interface and $V_{self}^{(plan)}(\sigma/2) = 0.95Z^2 k_B T$ for the planar one. These features can be physically explained in terms of polarization charges. In the contact region (i. e., for small θ - see Fig. 2) we know that the surface polarization charge is quasi-identical on both spherical and planar interfaces. However, for *finite* curvature we also know that $\sigma_{pol}^{(sph)}$ changes sign above θ^* and in the present case $\sigma_{pol}^{(sph)}$ gets *oppositely* charged to q . This latter effect is the main cause that leads to a weaker self-image interaction for spherical interfaces. Nevertheless, by increasing a (i.e., reducing the curvature) one approaches the planar case as expected (see Fig. 4). Physically, this means that the contribution of the negative polarization charges (lying at $\theta > \theta^*$) to the self-image interaction [Eq. (24)] becomes negligible for sufficiently large colloidal radius.

3. Effect of curvature on the contact potential

It is clear that for sufficiently low curvature one should recover the planar case as far as the self-image interaction is concerned. Thus, a natural question that arises is: for which typical colloidal size are curvature effects relevant?

A suitable observable for this problem is provided by the contact potential $V_{self}^{(sph)}(b = a + \sigma/2)$. This quantity is of special interest since it will correspond to the highest repulsive part of the global interaction between a macroion (i.e., *charged* macro-particle) and an oppositely charged counterion. In order to investigate the effect of finite curvature we are going to compare $V_{self}^{(sph)}(a + \sigma/2)$ to the contact potential $V_{self}^{(plan)}(b - a = \sigma/2)$ obtained with a planar interface.

The plot of the normalized contact potential $V_0^*(a)$ defined as

$$V_0^*(a) = \frac{V_{self}^{(sph)}(a + \frac{\sigma}{2})}{V_{self}^{(plan)}(\frac{\sigma}{2})} \quad (26)$$

can be found in Fig. 5. For the sake of numerical stability we used the formalism of Eq. (12) allowing an arbitrary precision.²⁰ Figure 5 shows that for a/σ larger than about 100 the contact potential is close to that of the planar interface (less than 5% difference). This length scale typically corresponds to “true” colloidal systems (~ 100 nm). Therefore, in the dilute regime where the self-image interaction is dominant (i.e. lateral microion-microion correlations are negligible), large-sized colloidal particles can be reasonably approximated by planar interfaces as far as the modeling of the self-image interaction is concerned. On the other hand, for a/σ smaller than about 20 the contact potential varies rapidly and therefore it is strongly dependent on the curvature. This length scale typically corresponds to micellar systems (~ 10 nm).

In this respect, Linse¹⁰ used an uncontrolled approximation where he replaced the (exact) infinite manifold of image charges [entering Eq. (12)] of total charge $-q_{im}$ by a single image point-charge $-q_{im}$ [given by Eq. (13)] located at the center of the sphere.²¹ Doing so the setup of image charges consists of a (two point-charge) dipole $\mathbf{p}_{im} = q_{im}\mathbf{u}$, and the corresponding contact potential $\tilde{V}_{self}^{(sph)}(r_0)$ reads

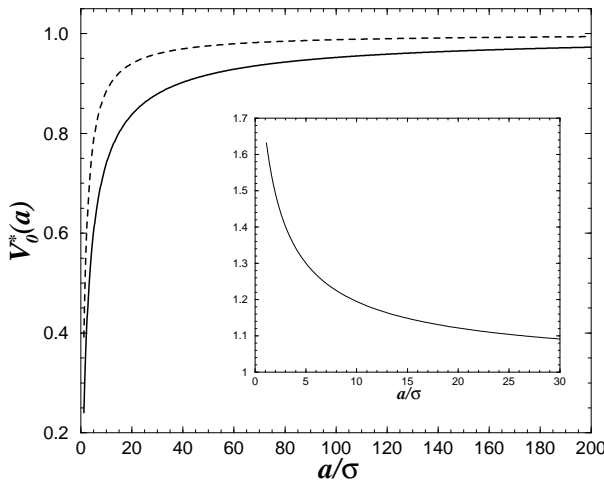


FIG. 5: Reduced contact potential $V_0^*(a)$ as a function of the colloidal radius a with $\varepsilon_1 = 80$, $\varepsilon_2 = 2$. The limit value of unity corresponds to the planar interface. The solid line is the exact contact potential $V_0^*(a)$ and the dashed one is the contact potential $\tilde{V}_0^*(a)$ obtained with the two-image charge approximation used by Linse.¹⁰ The insert shows the ratio $\tilde{V}_0^*(a)/V_0^*(a)$.

$$\tilde{V}_{self}^{(sph)}(b = r_0) = k_B T l_B \frac{Z^2}{2} \frac{\varepsilon_1 - \varepsilon_2}{\varepsilon_1 + \varepsilon_2} \frac{a}{r_0} \left[\frac{1}{r_0 - u} - \frac{1}{r_0} \right]. \quad (27)$$

The plot of

$$\tilde{V}_0^*(a) = \frac{\tilde{V}_0^{(sph)}(a + \frac{\sigma}{2})}{V_{self}^{(plan)}(\frac{\sigma}{2})} \quad (28)$$

can also be found in Fig. 5. It shows that the two-image charge approximation used by Linse is only valid for very low curvature (i.e., close to the planar case) and may strongly overestimate the self-image repulsion as expected by its inherent construction.²² In his MC simulations, Linse¹⁰ investigated micelles of radius $12 - 18$ Å (i.e., $a/\sigma \sim 3.5 - 5$) leading to errors as large as 40% (see insert of Fig. 5). This proves that this ansatz is unsuitable to determine the self-image interaction in this regime, which is the source of the image forces.

4. Charged colloid

As a last theoretical result, we consider the interaction between (a single counterion) q and a negatively charged dielectric sphere. The procedure is completely similar to the neutral colloid case, and we now apply the principle of superposition to take into account the additional potential due to a central charge $Q_m = -Z_m e$. The (global) macroion-counterion potential of interaction $V_m(b)$ reads

$$V_m(b) = -k_B T l_B \frac{Z_m Z}{b} + V_{self}^{(sph)}(b) \quad (29)$$

where $V_{self}^{(sph)}(b)$ is given by Eq. (23), and hence

$$V_m(b) = k_B T \frac{l_B}{b} Z^2 \left[-\frac{Z_m}{Z} + \frac{1}{2} \sum_{l=1}^{\infty} \left(\frac{a}{b} \right)^{2l+1} \frac{(\varepsilon_1 - \varepsilon_2)l}{\varepsilon_1(l+1) + \varepsilon_2 l} \right]. \quad (30)$$

Profiles of $V_m(b)$ for $Z_m = 60$, $r_0 = 8\sigma$, $\varepsilon_2 = 2$ and $Z = 1, 2$ and 3 are reported in Fig. 6. An important result is the occurrence of a *minimum* in $V_m(b)$ whose depth and position r^* increase with increasing Z . This is due to the purely *repulsive* self-image interaction which scales like Z^2 , whereas the direct *attractive* Coulomb macroion-microion interaction scales like Z (at fixed Z_m). Nevertheless the occurrence of a minimum is strongly dictated by the ratio Z_m/Z [see Eq. (30)]. For high value of Z_m/Z , $|V_m(b)|$ is maximal for $b = r_0$ (only *attraction* occurs) and for small Z_m/Z one recovers the neutral colloid case where only *repulsion* occurs. Of course the same

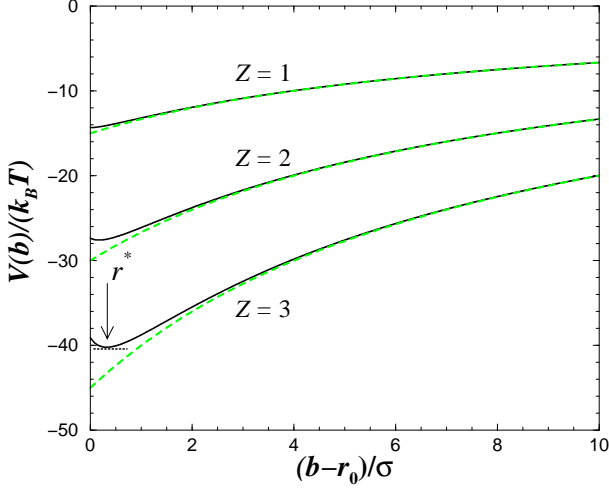


FIG. 6: Global macroion-counterion potential of interaction (solid lines) with $Z_m = 60$, $r_0 = 8\sigma$, $\varepsilon_1 = 80$ and $\varepsilon_2 = 2$. The values of the corresponding minima r^* can be found in Table II. The dashed lines correspond to the usual electrostatic potential of interaction without image forces (i.e., $\Delta\varepsilon = 0$).

qualitatively happens for charged plates.²³ The values of r^* minimizing $V_m(b)$ (with $b > r_0$) are given in Table II. The quantity r^* will be useful to discuss our simulation results that concern *many* counterions and where we also have the same macroion bare charge ($Z_m = 60$).

Keep in mind that all our results above concern a single microion. When *many* counterions come into play, other important effects might appear in principle. In particular, when the number of counterions near the macroion surface is very large the image forces are practically canceled by symmetry reason.²⁴ Clearly, by approaching the (perfect) spherical symmetry one asymptotically cancels the polarization charges everywhere on the macroion surface. This point shows that the discrete nature of the counterions is crucial for the existence of image charges in spherical geometry.²⁵ In planar geometry the situation is radically different, where one gets an amplified image force upon increasing the number of “surface” counterions.

TABLE II: Theoretical values of r^* minimizing the macroion-counterion potential of interaction (with $Z_m = 60$, $\varepsilon_1 = 80$, $\varepsilon_2 = 2$ and $r_0 = 8\sigma$). The corresponding profiles can be found in Fig. 6.

ε_2	$\Delta\varepsilon$	Z	$(r^* - r_0)/\sigma$
2	78	1	0
2	78	2	0.17
2	78	3	0.32

III. MONTE CARLO SIMULATION

Standard canonical MC simulations following the Metropolis scheme were used.^{28,29} The system we consider is similar to those studied in previous works.^{30,31,32} It is made up of two types of charged hard spheres: (i) a macroion of radius a with a bare charge $Q_m = -Z_m e$ (with $Z_m > 0$) and (ii) small microions (counterions and coions) of diameter σ with charge $q = \pm Z e$ to ensure the electroneutrality of the system. All these ions are confined in an impermeable cell of radius R and the macroion is held fixed at the center of the cell.

The dielectric media are modeled as in Sec II. The outer region of the simulation cell is assumed to have the same dielectric constant ε_1 as the solvent in order to avoid the appearance of artificial image forces.

The work done in bringing the (real) ions together from infinite separation gives the interaction energy of the system. The corresponding Hamiltonian, U_{tot} , can be expressed as

$$U_{tot} = \sum_i \left[U_i^{(m)} + \sum_{j>i} U_{ij}^{(bare)} \right] + \sum_i \left[U_i^{(self)} + \sum_{j>i} U_{ij}^{(im)} \right]. \quad (31)$$

The first two terms in Eq. (31) correspond to the traditional electrostatic interactions between real charges. More explicitly,

$$U_i^{(m)}(r_i) = \begin{cases} \pm l_B k_B T \frac{Z_m Z}{r_i}, & \text{for } r_i \geq a + \frac{\sigma}{2}, \\ \infty, & \text{for } r_i < a + \frac{\sigma}{2}, \end{cases} \quad (32)$$

represents the macroion-microion interaction, where (+) applies to coions and (-) to counterions, and

$$U_{ij}^{(bare)}(r_{ij}) = \begin{cases} \pm l_B k_B T \frac{Z^2}{r_{ij}}, & \text{for } r_{ij} \geq \sigma, \\ \infty, & \text{for } r_{ij} < \sigma, \end{cases} \quad (33)$$

the pair interaction between microions j and i where (+) applies to microions of the same type and (-) otherwise.

The two last terms in Eq. (31) account for the interaction between images and microions. The *repulsive* self-image interaction is given by

$$U_i^{(self)}(r_i) = \begin{cases} \frac{1}{2} k_B T l_B \frac{Z^2}{r_i} \sum_{l=1}^{l_{max}} \left(\frac{a}{r_i} \right)^{2l+1} \\ \times \frac{(\varepsilon_1 - \varepsilon_2)l}{\varepsilon_1(l+1) + \varepsilon_2 l}, & \text{for } r_i \geq a + \frac{\sigma}{2}, \\ \infty, & \text{for } r_i < a + \frac{\sigma}{2}, \end{cases} \quad (34)$$

where l_{max} is the cutoff in the Legendre space, and

$$U_{ij}^{(im)}(\mathbf{r}_i, \mathbf{r}_j) = \begin{cases} \pm l_B k_B T Z^2 \sum_{l=1}^{l_{max}} \frac{a^{2l+1}}{r_j^{l+1}} \frac{(\varepsilon_1 - \varepsilon_2)l}{\varepsilon_1(l+1) + \varepsilon_2 l} \\ \times \frac{1}{r_i^{l+1}} P_l(\cos \theta), & \text{for } r_i \geq a + \frac{\sigma}{2}, \\ \infty, & \text{for } r_i < a + \frac{\sigma}{2}, \end{cases} \quad (35)$$

represents the interaction between microion i and the image (surface charge induced by) of microion j , where (+) applies to charges of the same sign [and (-) otherwise] and θ is the angle between \mathbf{r}_i and \mathbf{r}_j . It is this term that generates *lateral* image-counterion correlations. Due to the symmetry of $U_{ij}^{(im)}$ upon exchanging ij with ji there is an implicit factor $1/2$ in Eq. (35).

Convergence of the Legendre sums with a relative error of 10^{-6} is obtained with the employed value of $l_{max} = 100$.³³ For the sake of computational efficiency and without loss of accuracy, we computed the image-ion interactions on a (very) fine $(r, \cos \theta)$ grid where the coordinates of the microions were extrapolated. The radial distances r_i are discretized over logarithmically equidistant nodes so that close to the macroion surface the radial resolution is 0.01σ and near the simulation wall 0.1σ . The polar discretization consists of 2000 equidistant $\cos \theta$ -nodes leading to even smaller lateral resolutions. The corresponding values of $U_i^{(self)}(r_i)$ and $U_{ij}^{(im)}(r_i, r_j, \cos \theta)$ were then initially stored into tables. Note that it in principle one could also have used the formalism of Eq. (12) to compute the image-ion interactions. However, at identical numerical accuracy, this method involving a numerical integration is too time and resource consuming.

Typical simulation parameters are gathered in Table III. The case $\varepsilon_2 = 80$ corresponds to the situation where

TABLE III: Model simulation parameters with some fixed values. Apart from the charge sign, counterions and coions have the same parameters.

Parameters	
$T = 298K$	room temperature
$\varepsilon_1 = 80$	water solvent dielectric constant
$\varepsilon_2 = 2$	colloidal dielectric constant
$\Delta\varepsilon = \varepsilon_1 - \varepsilon_2 = 78$	strength of dielectric discontinuity
Z_m	macroion valence
Z	counterion valence
$\sigma = 3.57 \text{ \AA}$	counterion diameter
$l_B = 2\sigma = 7.14 \text{ \AA}$	Bjerrum length
$a = 7.5\sigma$	macroion radius
$r_0 = a + \frac{\sigma}{2} = 8\sigma$	macroion-counterion distance of closest approach
R	radius of the outer simulation cell

there is *no* dielectric discontinuity ($\Delta\varepsilon = 0$). Measurements were performed over 10^6 MC steps per particle.

IV. SIMULATION RESULTS

Here we present our MC simulation results in salt-free environment as well as in the presence of multivalent salt-ions. We essentially study in detail the radial microion distributions $n_i(r)$ around the macroion, which are normalized as follows

$$\begin{cases} \int_{r_0}^R 4\pi r^2 n_+(r) dr = N_+ \\ \int_{r_0}^R 4\pi r^2 n_-(r) dr = N_-, \end{cases} \quad (36)$$

where r is the distance separation from the macroion center, +(-) stands for counterion (coion) species and N_+ (N_-) is the total number of counterions (coions) contained in the simulation cell.

Another quantity of special interest is the integrated (or cumulative) fluid net charge $Q(r)$ defined as

$$Q(r) = \int_{r_0}^r 4\pi u^2 Z [n_+(u) - n_-(u)] du, \quad (37)$$

where we chose $e = 1$. $Q(r)$ corresponds to the total fluid charge (omitting the macroion bare charge Z_m) within a distance r from the macroion center, and at the cell wall $Q(r = R) = Z_m$. Up to a factor proportional to $1/r^2$, $[Q(r) - Z_m]$ gives (by simple application of the Gauss theorem) the mean electric field at r . Therefore $Q(r)$ can measure the strength of the macroion charge screening by salt-ions. In salt-free environment systems we have $n_-(r) = 0$ and $N_+ = Z_m/Z$.

The simulation run parameters can be found in Table IV. For all these simulation systems, the ion densities $n_i(r)$ were computed with the same radial resolution Δr .³⁴ The discretization of the radial distance r in $n_i(r)$ is realized over logarithmically equidistant points so that close to the macroion surface ($r - r_0 < \sigma$) we have $\Delta r < 0.04\sigma$. It is important to obtain such an

TABLE IV: System parameters.

System	<i>A</i>	<i>B</i>	<i>C</i>	<i>D</i>	<i>E</i>	<i>F</i>	<i>G</i>	<i>H</i>	<i>I</i>	<i>J</i>
Z_m	60	60	60	60	60	60	60	60	180	180
Z	1	1	2	2	3	3	2	2	2	2
N_+	60	60	30	30	20	20	430	430	445	445
N_-	-	-	-	-	-	-	400	400	400	400
ε_2	2	80	2	80	2	80	2	80	2	80
$\Delta\varepsilon$	78	0	78	0	78	0	78	0	78	0
R/σ	40	40	40	40	40	40	20	20	20	20

accuracy (and the required statistics) if one wants to describe quantitatively the effects of image forces which are short-ranged at strong curvature.

A. Salt-free environment

Salt-free systems $A - F$ (see Table IV) were investigated for a moderately charged macroion $Z_m = 60$ corresponding to a surface charge density $\sigma_0 = 0.11 \text{ Cm}^{-2}$.

1. Monovalent counterions

The profiles of $n_+(r)$ and $Q(r)$ are depicted in Fig. 7(a) and (b), respectively for the monovalent counterion systems A and B .

Figure 7(a) shows that the counterion density at contact ($r = r_0$) is somewhat smaller with $\Delta\epsilon = 78$ as a direct consequence of the self-image repulsion. However there is no maximum appearing in $n_+(r)$ with $\Delta\epsilon = 78$, in agreement with the study of the single-counterion system (see Fig. 6 and Table II). For $r - r_0 > \sim 0.6\sigma$ (corresponding roughly to three half ionic sizes from the interface), the effects of image forces are negligible and all $n_+(r)$ curves are nearly identical.

To gain further insight into the effects of *lateral* image-counterion correlations, we have considered the same system A ($\Delta\epsilon = 78$) but omitted the correlational term $U_{ij}^{(im)}$ [Eq. (35)] in the total Hamiltonian U_{tot} [Eq. (31)]. Physically, this means that, on the level of the image force, each counterion sees uniquely its self-image interaction. Thereby, Fig. 7(a) shows that (i) the corresponding counterion density $n_+^{(self)}(r)$ is nearly identical to $n_+(r)$, and (ii) in the vicinity of the interface $n_+^{(self)}(r)$ is slightly smaller than $n_+(r)$. These findings (i) and (ii) lead to the two important conclusions:

- For monovalent counterions and moderately charged macroions, the *effective* image force is basically identical to that of the self-image interaction.³⁵
- The crucial effect of lateral image-counterion correlations is to *screen* the self-image repulsion.

This latter feature is generally true for any *finite* curvature at identical fixed macroion charge density. Finding (i) is also consistent with the fact that, close to the interface (say $r - r_0 < 0.2\sigma$), the average number of (surface) counterions \bar{N} is (very) small ($\bar{N} < 5$) as can be deduced from the fraction of counterions $Q(r)/Z_m$ [Fig. 7(b)].

Figure 7(b) shows that the fluid charge $Q(r)$ decreases when image forces are present, meaning that they lower the macroion charge screening by counterions. At the distance $r - r_0 = \sigma$ (corresponding to a 2σ -layer thickness), the macroion is 29% electrically compensated [i.e., $Q(r - r_0 = \sigma)/Z_m = 0.29$] with $\Delta\epsilon = 0$ against 26% with

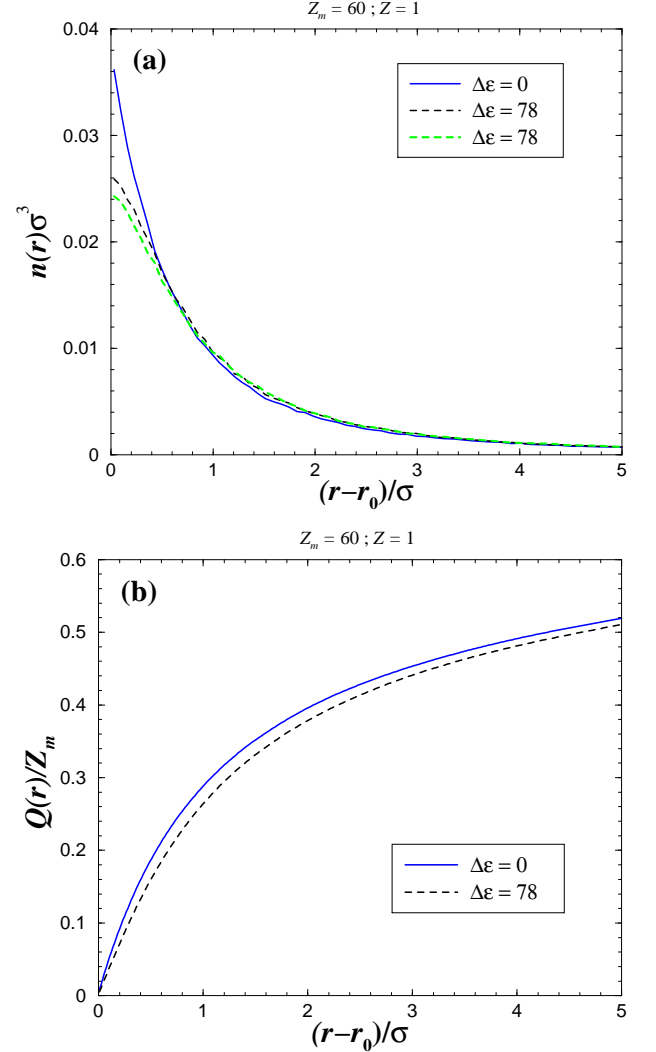


FIG. 7: Monovalent counterion distributions (systems A and B): (a) density $n_+(r)$. The dashed line in grey corresponds to the counterion density $n_+^{(self)}(r)$ obtained in the same system A ($\Delta\epsilon = 78$) but where the (lateral) image-counterion correlational term $U_{ij}^{(im)}$ [Eq. (35)] has been omitted in the total Hamiltonian U_{tot} [Eq. (31)]. (b) fluid charge.

$\Delta\epsilon = 78$. At the distance $r - r_0 = 4\sigma$, the relative difference $\Delta Q/Q$ between the $Q(r)$ obtained with $\Delta\epsilon = 0$ and $\Delta\epsilon = 78$ drops to 2% (against 10% at $r - r_0 = \sigma$) where the bare macroion charge is nearly half-compensated.

2. Multivalent counterions

a. Divalent counterions The profiles of $n_+(r)$ and $Q(r)$ are depicted in Fig. 8(a) and (b), respectively for the divalent counterion systems C and D .

Figure 8(a) shows that the counterion density at contact becomes strongly reduced with $\Delta\epsilon = 78$ due to the Z^2 -dependence of the self-image repulsion [compare the

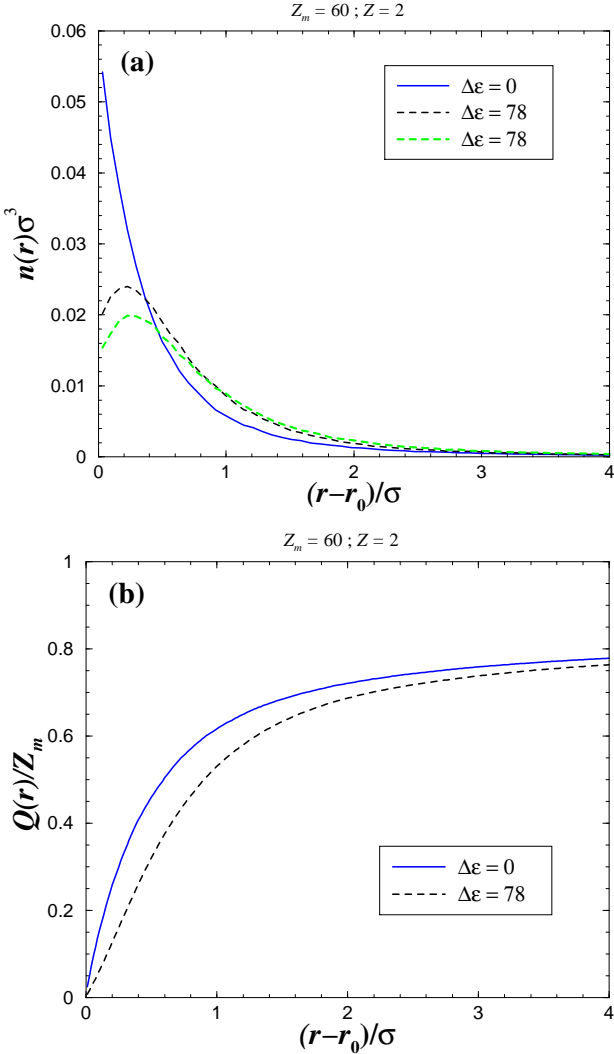


FIG. 8: Divalent counterion distributions (systems *C* and *D*): (a) density $n_+(r)$. The dashed line in grey corresponds to the counterion density $n_+^{(self)}(r)$ obtained in the same system *C* ($\Delta\epsilon = 78$) but where the (lateral) image-counterion correlational term $U_{ij}^{(im)}$ [Eq. (35)] has been omitted in the total Hamiltonian U_{tot} [Eq. (31)]. (b) fluid charge.

case $Z = 1$ in Fig. 7(a)]. This sufficiently strong (short-ranged) repulsion leads to a maximum in $n_+(r)$ close to the macroion surface. The corresponding radial position r^* maximizing $n_+(r)$ is $r^* = r_0 + 0.22\sigma$, in excellent agreement (within Δr) with the *one-counterion* theoretical value $r_0 + 0.17\sigma$ (see Table II). This shows that for divalent counterions many-body effects do nearly not affect r^* . This non-trivial finding is the result of the competition between two driving forces that control r^* in *many*-counterion systems:

- F_{im} : the screening of the self-image *repulsion* by the (extra) negative polarization charges tends to *decrease* the r^* obtained in the one-counterion system.

- F_{mc} : the screening of the macroion-counterion *attraction* by the (extra) surface counterions tends to *increase* the r^* obtained in the one-counterion system.

It is precisely a balance of these two driving forces that leads to a nearly unchanged r^* (compared to the one-counterion system) in many-counterion systems. Whereas for monovalent counterions both driving forces F_{im} and F_{mc} are weak, those become relevant for multivalent counterions.

We stress the fact that this is specific to the spherical geometry, and that for a planar interface (at identical surface charge density) one should get a higher r^* (compared to that of the one-counterion system), since there we have no screening driving force F_{im} . We are not aware of any previous studies for the planar interface that address this issue.³⁶

To gain even further insight into the effect of Z on the lateral image-counterion correlations, we have ignored the term $U_{ij}^{(im)}$ in U_{tot} in the same system *D* ($\Delta\epsilon = 78$) as done previously with system *A*. Figure 8(a) shows a qualitatively different $n_+^{(self)}(r)$ where $r^* = r_0 + 0.26\sigma$ is now somewhat larger, proving that with divalent counterions the screening of the self-image repulsion by lateral image-counterion correlations is appreciable. This is in contrast to what was observed with $Z = 1$.

At the distance $r - r_0 = \sigma$, Fig. 8(b) shows that the macroion is 62% electrically compensated for $\Delta\epsilon = 0$ against 53% for $\Delta\epsilon = 78$ [compare the case $Z = 1$ in Fig. 7(b)].

b. Trivalent counterions The profiles of $n_+(r)$ and $Q(r)$ are depicted in Fig. 9(a) and (b), respectively for trivalent counterion systems *E* and *F*.

Figure 9(a) shows that the counterion density at contact is drastically reduced with $\Delta\epsilon = 78$, as expected for high Z (compare the previous cases). At $\Delta\epsilon = 78$, we have $r^* = r_0 + 0.36\sigma$, in quantitative agreement with the *one-counterion* theoretical value $r_0 + 0.32\sigma$ (see Table II). This shows again that even for trivalent counterions many-body effects do (practically) not affect r^* (compared to that obtained in the single-counterion system) due to a balance of the driving forces F_{im} and F_{mc} .

By neglecting the lateral image-counterion correlations in the same system *E* ($\Delta\epsilon = 78$), Fig. 9(a) indicates that the position r^* of the maximum in $n_+^{(self)}(r)$ gets considerably larger ($r^* = r_0 + 0.50\sigma$). This relatively strong shift confirms the Z -enhancing of the screening of the self-image repulsion by lateral image-counterion correlations.

At the distance $r - r_0 = \sigma$, the macroion is 84% electrically compensated for $\Delta\epsilon = 0$ against only 67% for $\Delta\epsilon = 78$ [see Fig. 9(b) and compare previous systems]. Snapshots of typical equilibrium configurations for $\Delta\epsilon = 0$ and $\Delta\epsilon = 78$ can be visualized in Fig. 10 (a) and (b), respectively.

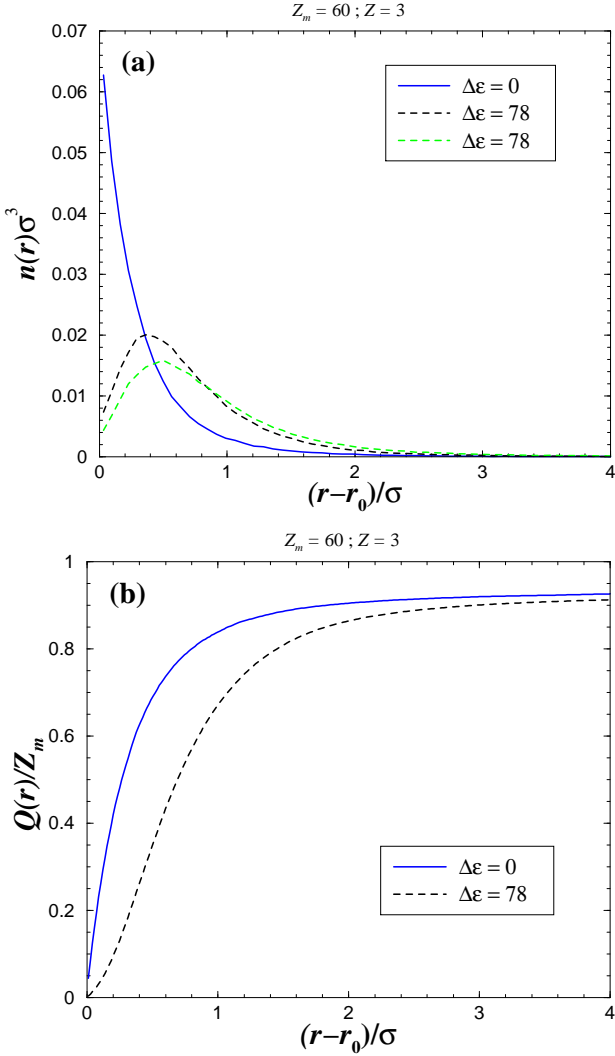


FIG. 9: Trivalent counterion distribution (systems E and F): (a) density $n_+(r)$. The dashed line in grey corresponds to the counterion density $n_+^{(self)}(r)$ obtained in the same system E ($\Delta\epsilon = 78$) but where the (lateral) image-counterion correlational term $U_{ij}^{(im)}$ [Eq. (35)] has been omitted in the total Hamiltonian U_{tot} [Eq. (31)]. (b) fluid charge.

B. Salty solutions

We focus on the case of divalent salt-ions. This choice is motivated by two reasons: (i) effects of image charges are clearly observable for multivalent counterions and (ii) such systems must be experimentally reachable. To study the effect of added salt we have considered two macroion charges $Z_m = 60$ (as previously) and $Z_m = 180$ corresponding to a charge density $\sigma_0 = 0.32 \text{ Cm}^{-2}$. The salt concentration defined as $\frac{N_-}{\frac{4}{3}\pi R^3}$ is 0.44 M for all salty systems $G - J$ (see Table IV). The simulation cell radius $R = 20\sigma$ of these systems is still very large compared to any screening lengths so that finite size effects are negligible.

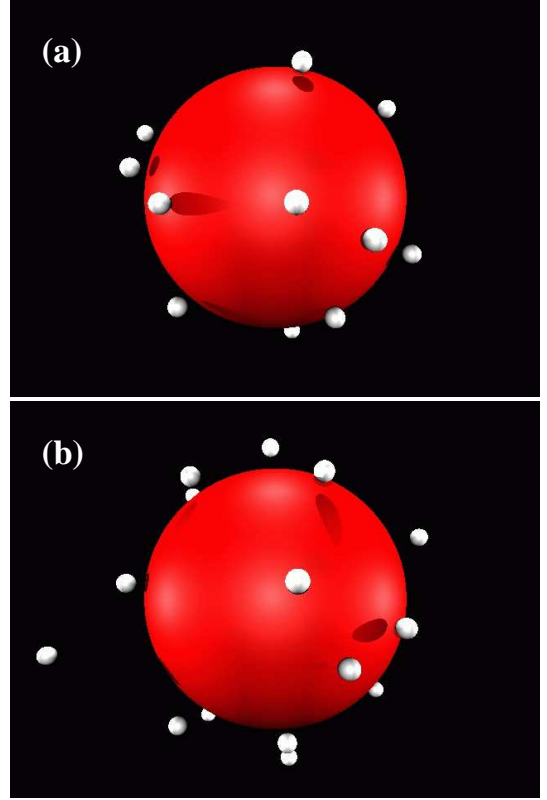


FIG. 10: Snapshots of typical equilibrium configurations for trivalent counterions (systems E and F). (a) $\Delta\epsilon = 0$ (b) $\Delta\epsilon = 78$. One can clearly observe the larger mean radial counterion distance for $\Delta\epsilon = 78$ stemming from the self-image repulsion.

1. Moderately charged macroion

Profiles of $n_\pm(r)$ and $Q(r)$ are depicted in Fig. 11(a) and (b), respectively for the salty systems G and H with $Z_m = 60$.

The coion density $n_-(r)$ with $\Delta\epsilon = 78$ is basically shifted to the right of about 0.15σ (compared to that with $\Delta\epsilon = 0$) due to the repulsive coion' self-image interaction. Near the colloidal surface, the counterion densities $n_+(r)$ are considerably higher than those obtained with no added salt (systems C and D) as it should be [compare Fig. 8(a)].

A rather surprising result here is that, despite of the presence of a considerable amount of added salt, we still have $r^* = r_0 + 0.22\sigma$ remaining unchanged. This is a non-trivial finding since one should have an (extra) *attractive* contribution to the macroion-counterion potential of mean force stemming from the (localized) *negative* polarization charges induced by the coions, which in turn could lead to a shorter r^* . However there are two concomitant sources that lead to a marginal screening of the counterion' self-image repulsion by the negative coion-induced polarization charges: (i) there is a strong coion depletion close to the interface [see Fig. 11(a)] due to

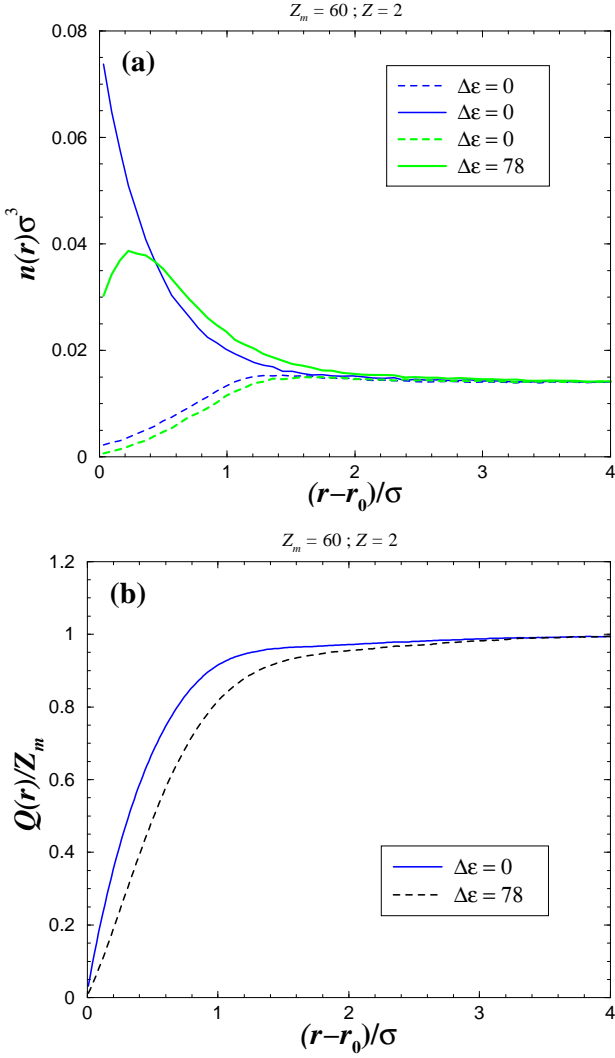


FIG. 11: Divalent salt-ion distribution (systems *G* and *H*) with $Z_m = 60$: (a) The solid and dashed lines correspond to counterion and coion densities, respectively. (b) net fluid charge.

the large direct Coulomb macroion-coion repulsion and (ii) $|\sigma_{pol}^{(sph)}|$ decreases abruptly with the radial distance of the microion as discussed in Sec. II D 1 (see also Fig. 3). Of course the role of the *excluded volume* is crucial here.

As expected the macroion charge screening is weaker when image forces come into play as can be deduced from the profile of $Q(r)$ plotted in Fig. 11(b).

2. Highly charged macroion

Profiles of $n_{\pm}(r)$ and $Q(r)$ are depicted in Fig. 12(a) and (b), respectively for the salty systems *I* and *J* with $Z_m = 180$.

Figure 12(a) shows that the effects of image forces are considerably reduced. The relatively small difference be-

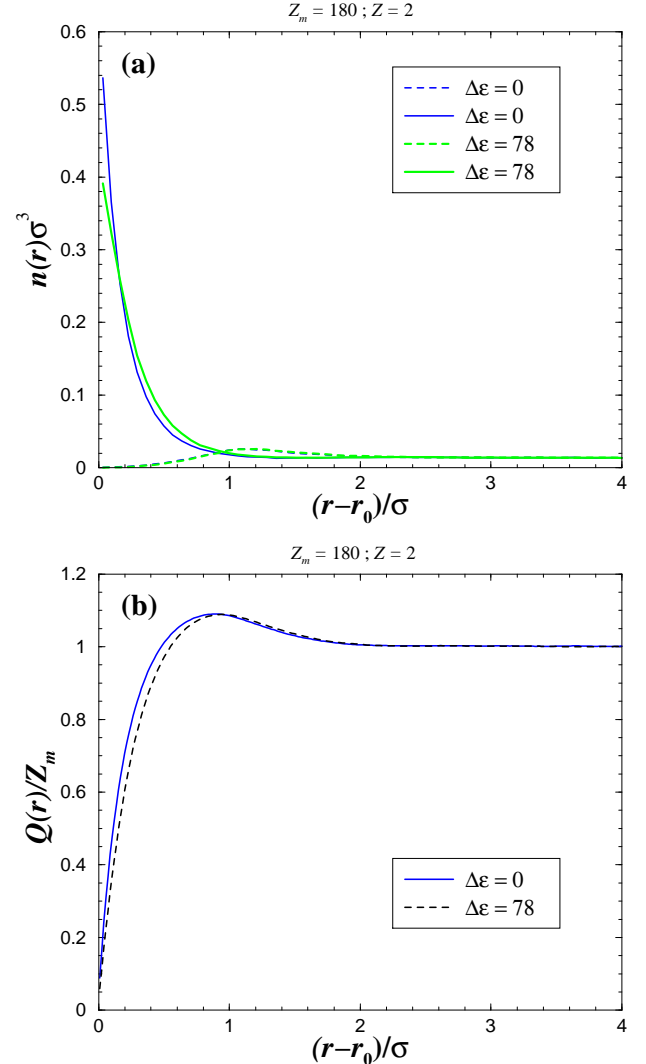


FIG. 12: Divalent salt-ion distribution (systems *I* and *J*) with $Z_m = 180$: (a) The solid and dashed lines correspond to counterion and coion densities, respectively. (b) net fluid charge.

tween the $n_+(r)$ obtained with $\Delta\epsilon = 0$ and that obtained with $\Delta\epsilon = 78$ decreases drastically in the vicinity of the interface, and already for $r - r_0 > \sim 0.2\sigma$ the two profiles of $n_+(r)$ are nearly identical. Besides, near the interface no effective macroion-counterion repulsion occurs at $\Delta\epsilon = 78$. This absence of a maximum in $n_+(r)$ is due to two main concomitant effects:

- For such a highly charged macroion, there is a very large number of counterions close to the interface [compare Fig. 12(b) and Fig. 11(b)]. In this limit, one can use Wigner crystal concepts and say that, on the level of the force stemming from the bare charges (i.e, ignoring the image forces), each surface counterion essentially interacts with the oppositely charged background of its Wigner-Seitz (WS) cell. At sufficiently high macroion charge density (i.e.,

small WS hole radius), this attractive interaction becomes very important and it always overcomes the self-image repulsion.

- The second (concomitant) mechanism is specific to the closed spherical topology: at high number of surface counterions, the image forces are reduced because of the enhanced degree of spherical symmetry as already mentioned in Sec. II D 4.

The coion densities $n_-(r)$ are basically identical for both dielectric discontinuities $\Delta\epsilon$, in contrast to what happened with $Z_m = 60$ (systems *J* and *K*). This non-trivial finding can be explained as the enhanced screening of the coion' self-image repulsion by the positive polarization charges induced by the other coions present in the electrical double layer (EDL). Indeed, because of the macroion charge reversal that occurs at $Z_m = 180$ [i.e., $Q(r)/Z_m > 1$ - see Fig. 12(b)], there is also a larger number of coions (at fixed salt concentration) in the EDL [compare Fig. 12(a) and Fig. 11(a)]. Therefore, since the magnitude and the inhomogeneity of $-\sigma_{pol}^{(sph)}(\theta)$ induced by a coion strongly decreases with its radial distance [see Eq. (16) and Fig. 3], the screening of the coion' self-image repulsion gets highly sensitive to an increase in number of coions in the EDL.

Concerning the net fluid charge $Q(r)$, we see that both profiles obtained with $\Delta\epsilon = 78$ and $\Delta\epsilon = 0$ are nearly identical, as expected from those of $n_{\pm}(r)$. The net fluid charge $Q(r)$ reaches its maximum at $r_Q^* - r_0 = 0.90\sigma$ and 0.94σ for $\Delta\epsilon_2 = 0$ and 78 , respectively. In both cases we have a macroion charge reversal of 9% [more explicitly $Q(r_Q^*)/Z_m = 1.09$]. This proves the important result that, for typical systems (with high macroion charge density) leading to overcharging,^{26,27,30,31,32} image forces do not affect the strength of the macroion charge reversal.

V. CONCLUDING REMARKS

We have presented fundamental results about the effects of image forces on the counterion distribution around a spherical macroion.

Exact analytical results have been provided for the case of a single microion interacting with a dielectric sphere. Within this framework, the self-image interaction and the surface charge of polarization have been studied and also compared to those obtained with a planar interface. Besides we also estimated the position r^* where the macroion-counterion potential of interaction is minimized. We demonstrated that the effects of image forces due to a spherical interface are qualitatively different from those occurring with a planar interface, especially when the colloidal curvature is large. We showed that the *self-screening* of the polarization charges (i.e., the screening of the positive surface charges of polarization by the negative ones) is decisive to explain the weaker and the shorter range of the self-image interac-

tion in spherical geometry. This self-screening increases with the colloidal curvature.

Many-counterion systems have been investigated by means of extensive MC simulations where image forces were properly taken into account.

In salt-free environment and for moderately charged macroions, a maximum in the counterion density (near the spherical interface) appears for sufficiently large dielectric discontinuity $\Delta\epsilon$. An important result is that the corresponding position r^* is basically identical, regardless of the counterion valence Z , to that obtained within the one-counterion system. This feature is specific to the spherical geometry and can not take place with planar interfaces where there is *no* self-screening of the polarization charges. For monovalent counterions we showed that the (effective) image force is basically equal to that of the self-image interaction, and the *lateral* image -counterion correlations are (very) weak. However for multivalent counterions the lateral image-counterion correlations affect significantly the counterion density, and as major effect they *screen* the self-image repulsion. Nevertheless, the combined effects of (i) the macroion charge screening by counterions and (ii) the screening of the self-image repulsion lead to a nearly unchanged r^* (compared to that obtained in the single-counterion system) for multivalent many-counterion systems. We also showed that the counterion density at contact decreases drastically with Z , and that r^* also increases with Z as expected. These latter results have important implications for the stabilization of charged colloidal suspensions where a component of the pair-force is proportional to the ion density at contact.

By adding salt, it was found for moderately charged macroions that the strength of the image forces induced by the *coions* is very small compared to that resulting from the counterions. This is due to the coupled effects of (i) the coion depletion in the vicinity of the colloidal interface due to the strong direct Coulomb macroion-coion repulsion and (ii) the (highly) short range of the image forces in spherical geometry. Consequently the position r^* remains identical to that obtained in salt free environment and a fortiori to that obtained within the one-counterion system. For *highly* charged macroions the effects of image charges are significantly reduced since (i) the attractive counterion-hole interaction dominates the repulsive counterion' self-image interaction and (ii) the screening of the counterion' self-image repulsion gets enhanced by symmetry reason. In this situation *no* maximum appears in the counterion density and it was found that *overcharging* is nearly unaffected by image forces.

Although our MC analysis was carried at given macroion size, all the above reasonings that concern *many* counterions remain unchanged (for symmetry reason) for any *finite* curvature by a rescaling at fixed macroion charge density.

Finally, this contribution should constitute a solid basis to understand and predict the effects of image charges in other similar systems (e.g., polyelectrolyte adsorption

onto spherical charged colloids).

oratoires Européens Associés (LEA).

Acknowledgments

I thank C. Holm, K. Kremer and H. Schiessel for valuable discussions. This work had been supported by *Lab-*

^{*} Electronic address: messina@mpip-mainz.mpg.de

¹ G. M. Torrie, J. P. Valleau, and G. N. Patey, *J. Chem. Phys.* **76**, 4615 (1982).

² G. M. Torrie, J. P. Valleau, and C. W. Outhwaite, *J. Chem. Phys.* **81**, 6296 (1984).

³ D. Bratko, B. Jönsson, and H. Wennerström, *Chem. Phys. Lett.* **128**, 449 (1986).

⁴ T. Croxton *et al.*, *Can. J. Chem.* **59**, 1998 (1981).

⁵ R. Kjellander and S. Marčelja, *Chem. Phys. Lett.* **112**, 49 (1984).

⁶ R. Kjellander and S. Marčelja, *J. Chem. Phys.* **82**, 2122 (1985).

⁷ C. W. Outhwaite and L. B. Bhuiyan, *J. Chem. Soc. Faraday Trans. II* **79**, 707 (1983).

⁸ R. R. Netz, *Phys. Rev. E* **60**, 3174 (1999).

⁹ H. H. von Grünberg and E. C. Mbamala, *J. Phys. Condens. Matter* **12**, 10349 (2000).

¹⁰ P. Linse, *J. Phys. Chem.* **90**, 6821 (1986).

¹¹ Equation (5) is also of the form of Eq. (3).

¹² J. G. Kirkwood, *J. Chem. Phys.* **2**, 351 (1934).

¹³ M. R. Spiegel, *Fourier Analysis with applications to boundary value problems* (McGraw-Hill, New York, 1974).

¹⁴ J. D. Jackson, *Classical Electrodynamics* (Wiley, New York, 1975).

¹⁵ G. Iversen, Y. I. Kharkats, and J. Ulstrup, *Molec. Phys.* **94**, 297 (1998).

¹⁶ Note that for $\varepsilon_2 \rightarrow \infty$ in Eq. (12) one recovers the case of a metallic *conducting* sphere where there is a *single* image point-charge $q_{im} = -qa/b$ located at \mathbf{u} .

¹⁷ Mathematically, this is a direct consequence of the orthogonality of the Legendre polynomials. Indeed, we have $\int_{-1}^1 P_l(x)P_0(x)dx = 0$ and since $P_0(x) = 1$ it results from this that $\int_{-1}^1 P_l(x)dx = 0$.

¹⁸ It turns out that the convergence of the Legendre sum in Eq. (16) is extremely slow. With $l_{max} = 300$ we have a relative error of 10^{-6} in the most severe case where $b = 8\sigma$.

¹⁹ This holds when the microion q is sufficiently far away from the interface so that only the dipolar term matters (i.e., $l = 1$). However close to the colloidal surface one has to take all higher multipolar contributions to get the exact potential of interaction.

²⁰ We have carefully checked that both methods [i.e., Eq. (10) and Eq. (12)] are numerically identical. However, at large a (typically $a > 30\sigma$) the Legendre sum in Eq. (23) becomes numerically unstable.

²¹ Originally, Linse¹⁰ made some manipulations in the Legendre expansion and drops all l components after having approximated $\frac{1}{\varepsilon_1 + \varepsilon_2 l/(l+1)} \approx \frac{1}{\varepsilon_1 + \varepsilon_2}$. This operation equivalents to replace the (exact) infinite manifold of image charges [entering Eq. (12)] by a single image point-charge $-q_{im}$ located at the center of the sphere.

²² Note that the two-image charge approximation also holds when the charge q is very far from the interface (i.e., $b/a \gg 1$). Unfortunately, all the relevant effects of image forces in spherical geometry occur within the opposite limit $b/a \rightarrow 1$.

²³ In the case of a charged plate, to be consistent, one has to think either of a large finite plate in the presence of a single microion, or equivalently of an infinite plate in the presence of a very dilute dispersion of microions.

²⁴ C. Holm (private communication).

²⁵ This problem is very similar, in spirit, to that of the discretization of the macroion surface charge whose effect is (asymptotically) canceled for small separations between microions.^{26,27}

²⁶ R. Messina, C. Holm, and K. Kremer, *Eur. Phys. J. E* **4**, 363 (2001).

²⁷ R. Messina, *Physica A* **308**, 59 (2002).

²⁸ N. Metropolis *et al.*, *J. Chem. Phys.* **21**, 1087 (1953).

²⁹ M. P. Allen and D. J. Tildesley, *Computer Simulations of Liquids* (Clarendon Press, Oxford, 1987).

³⁰ R. Messina, C. Holm, and K. Kremer, *Phys. Rev. Lett.* **85**, 872 (2000).

³¹ R. Messina, C. Holm, and K. Kremer, *Europhys. Lett.* **51**, 461 (2000).

³² R. Messina, C. Holm, and K. Kremer, *Phys. Rev. E* **64**, 021405 (2001).

³³ Here, the convergence of the Legendre sum in Eqs. (34) and (35) is much faster, in contrast to what happened with the computation of $\sigma_{pol}^{(sph)}(\theta)$ [Eq. (16)]. The most sensitive region is the one where $r \rightarrow r_0$. There, for $r_0 = 8\sigma$ we have a relative error of 10^{-6} with $l_{max} = 100$.

³⁴ For the net fluid charge $Q(r)$ one has an arbitrary resolution Δr .

³⁵ This feature also shows how important it is to treat precisely the self-image interaction as done in the present study with a Legendre sum.

³⁶ Using MC simulations, Torrie *et al.*¹ also reported in the planar case the appearance of a maximum in the counterion density for low surface charge density and fairly small salt content. However, they did not make any comparison between the position of this maximum and the position of a single counterion (per simulation box) minimizing the plate-counterion potential of interaction.